Chemical Science

EDGE ARTICLE

View Article Online
View Journal | View Issue

Cite this: *Chem. Sci.*, 2018, **9**, 5646

Sonophore-enhanced nanoemulsions for optoacoustic imaging of cancer†

Sheryl Roberts,‡[a] Chrysafis Andreou,‡[a] Crystal Choi,[a] Patrick Donabedian,[a] Madhumitha Jayaraman,[a] Edwin C. Pratt,[b] Jun Tang,[c] Carlos Pérez-Medina,[d] M. Jason de la Cruz,[e] Willem J. M. Mulder,[df] Jan Grimm,[abgh] Moritz Kircher[abg] and Thomas Reiner*[ag]

Optoacoustic imaging offers the promise of high spatial resolution and, at the same time, penetration depths well beyond the conventional optical imaging technologies, advantages that would be favorable for a variety of clinical applications. However, similar to optical fluorescence imaging, exogenous contrast agents, known as sonophores, need to be developed for molecularly targeted optoacoustic imaging. Despite numerous optoacoustic contrast agents that have been reported, there is a need for more rational design of sonophores. Here, using a library screening approach, we systematically identified and evaluated twelve commercially available near-infrared (690–900 nm) and highly absorbing dyes for multi-spectral optoacoustic tomography (MSOT). In order to achieve more accurate spectral deconvolution and precise data quantification, we sought five practical mathematical methods, namely direct classical least squares based on UV-Vis (UV/Vis-DCLS) or optoacoustic (OA-DCLS) spectra, non-negative LS (NN-LS), independent component analysis (ICA) and principal component analysis (PCA). We found that OA-DCLS is the most suitable method, allowing easy implementation and sufficient accuracy for routine analysis. Here, we demonstrate for the first time that our biocompatible nanoemulsions (NEs), in combination with near-infrared and highly absorbing dyes, enable non-invasive *in vivo* MSOT detection of tumors. Specifically, we found that NE-IRDye QC1 offers excellent optoacoustic performance and detection compared to related near-infrared NEs. We demonstrate that when loaded with low fluorescent or dark quencher dyes, NEs represent a flexible and new class of exogenous sonophores suitable for non-invasive pre-clinical optoacoustic imaging.

Received 13th April 2018
Accepted 14th May 2018

DOI: 10.1039/c8sc01706a

rsc.li/chemical-science

Introduction

The optoacoustic effect – the generation of sound waves by molecules upon absorbance of light – provides a new window for biomedical imaging that combines the resolution and molecular specificity of optical imaging with a much improved penetration depth. This combination makes it a valuable tool for a variety of preclinical and clinical applications. Although the photoacoustic effect was originally discovered in gases by Alexander Graham Bell in 1880 and reported in solids almost a century later,[1] it is only in the last decade that its use has been leveraged for biomedical imaging.[2,3] When implemented in a configuration that allows for multispectral optoacoustic tomography (MSOT), a rich image can be acquired, comprised of spatial, spectral, and temporal information.

Many molecules can be used for biomedical optoacoustic imaging, as long as they absorb light. These molecules, known as sonophores, can have endogenous or exogenous provenance. Hemoglobin, an endogenous sonophore, can be used to map out healthy or neoplastic vasculature,[4] hemorrhages,[5] and hematomas,[6] whereas the marked spectral difference between oxygenated and deoxygenated hemoglobin can be employed to monitor the oxygenation of blood or tissue.[7,8] Melanin has been used for imaging and detection of melanoma,[9] lymph node metastases,[10] and even melanoma metastases in-transit.[11] However, optoacoustic imaging with endogenous agents is currently limited to only a small subset of clinical conditions.

[a]*Department of Radiology, Memorial Sloan Kettering Cancer Center, New York, NY, 10065, USA. E-mail: reinert@mskcc.org*
[b]*Department of Molecular Pharmacology, Memorial Sloan Kettering Cancer Center, New York, NY, 10054, USA*
[c]*Cancer Research Institute (CRI), 29 Broadway, New York, NY, 10006, USA*
[d]*Translational and Molecular Imaging Institute, Department of Radiology, Mount Sinai School of Medicine, New York, NY, 10029, USA*
[e]*Structural Biology Program, Sloan Kettering Institute, Memorial Sloan Kettering Cancer Center, New York, New York, 10065, USA*
[f]*Department of Medical Biochemistry, Academic Medical Center, Amsterdam, The Netherlands*
[g]*Department of Radiology, Weill Cornell Medical College, New York, NY 10065, USA*
[h]*Pharmacology Program, Weill Cornell Medical College, New York, NY, 10065, USA*
† Electronic supplementary information (ESI) available. See DOI: 10.1039/c8sc01706a
‡ These authors contributed equally to this work.

Applications such as the tracking of cancer biomarkers, transiently expressed receptors and analytes, or disease-specific physiological changes other than oxygenation require the use of exogenous, molecularly targeted imaging agents.[12,13] Such agents need to provide a biologically orthogonal optoacoustic signal that is strong enough to overcome the high background of intrinsic sonophores. Also, excitation with near-infrared is preferable to visible light, as it is absorbed less by biological tissues, allowing for greater penetration depths. As such, small molecule NIR fluorescent dyes, most often indocyanine green (ICG), have been used as optoacoustic contrast agents for the imaging of tumors,[14] sentinel lymph nodes,[9,15,16] and vasculature.[17–19] Fluorescent dyes are generally suboptimal sonophores, as a substantial part of the absorbed energy dissipates radiatively at the expense of the optoacoustic signal (Fig. 1a).

Recently, in an effort to identify optimal sonophores, focus has shifted towards the development of dark quenchers or similar optoacoustically active constructs.[20–24] Unlike fluorescent dyes, dark quenchers dissipate a larger fraction of the absorbed light energy *via* non-radiative relaxation.[12]

One major challenge for hydrophobic small molecule dyes, fluorescent and quenchers alike, is their administration to the patient, often yielding unfavorable delivery pharmacokinetics to the region of interest. To circumvent this issue, nanoparticle based constructs can be used to encapsulate them.[25] Nanoparticles (NPs) can be functionalized in a multitude of fashions, enabling specific targeting, multimodal imaging, or theranostic applications.[26] Examples of NP-based sonophores have already been reported in preclinical studies of cancer imaging.[27,28] Additionally, when it comes to the imaging of cancer, NPs are well suited, as they accumulate in tumors *via* the enhanced permeability and retention (EPR) effect.[29–31] Although few NP agents have (so far) achieved approval for clinical use by regulatory bodies, increasing numbers of such agents are undergoing clinical trials.[31–33]

Here, we present the development and validation of a library of optoacoustic contrast agents based on oil-in-water nanoemulsions (NEs, Fig. 1b). We first employed twelve commercially available low fluorescent dyes and dark quenchers based on high extinction coefficients, and systematically compared their performance in tissue mimicking phantoms. Subsequently, we compared different methods of spectral deconvolution for specificity, focusing on signal quantitation. Lastly, we validated the performance of two of the NEs *via ex vivo* and *in vivo* optoacoustic imaging of tumors in a subcutaneous breast cancer allograft mouse model.

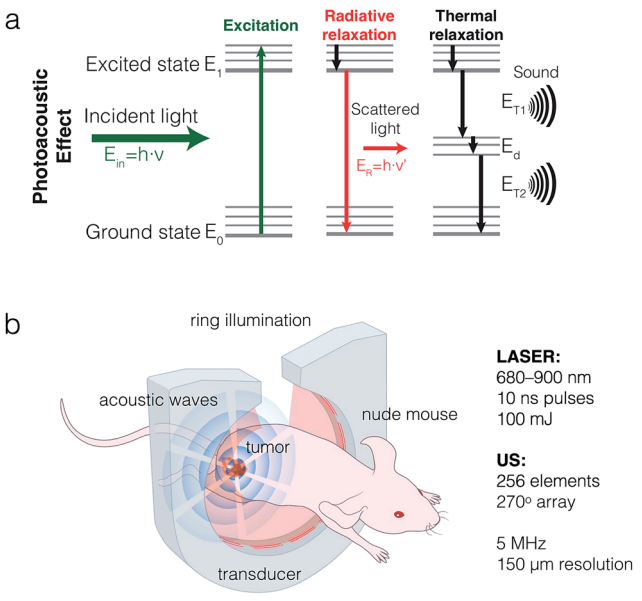

Fig. 1 Principle and experimental setup of optoacoustic imaging. (a) Sonophores absorb light upon laser excitation and undergo non-radiative and radiative relaxations. Non-radiative relaxation (rotational and vibrational) causes local heating, and in turn thermoelastic expansion, which generates acoustic waves. (b) The multi-spectral optoacoustic tomography (MSOT) setup surrounds the sample with a ring laser illuminator and ultrasound transducer in a 270° array. Tunable excitation wavelength (680–900 nm) allows spectral unmixing of intrinsic and extrinsic sonophores.

Results

Nanoemulsion synthesis and characterization

We synthesized a library of 12 NEs for MSOT screening, 9 of which are fluorescent dyes and three of which are dark quenchers, described in detail in the Methods section. The chemical structures of the dyes are shown in Fig. S1† and their extinction coefficient (ε) were reported in Fig. S2.† Briefly, stable NIR NEs were formulated *via* solvent displacement, as shown in Fig. 2a, adapting a previously described method.[34] The NEs had a minimum effective diameter of 119 nm ± 8.5 nm and a maximum effective diameter of 149 nm ± 5.8 nm with particle concentrations ranging from 0.23 to 0.75 nM, zeta potentials between −0.24 and −7.46 mV and PDI ≤ 0.15. Shown in Fig. 2 and in Fig. S3,† the nanostructure and homogeneous morphology of NE-IRDye QC1 was determined by cryogenic transmission electron microscopy (cryo-TEM). For the different dyes, we obtained encapsulation yields ranging between 0.43–16% (Table S1†). The yield and amount of dye encapsulated for selected NEs are shown in Fig. 4a. Physical characterization of the NEs and their corresponding dyes free in DMSO solution are summarized in Table S1.†

Additionally, we monitored the stability of the near-infrared dyes and corresponding nanoemulsions in native formulation (PBS) and in bovine serum albumin (BSA) by tracking their absorbance and photophysical properties over time. The size of the nanoemulsions in PBS shows little (<5%) or no change over the testing course of 30 days (Fig. S4†); with similar results obtained in serum over 24 h (Fig. S5†). The photostability of the near-infrared dyes and corresponding nanoemulsions was examined in both PBS and in BSA over the course of 15 days and 30 days respectively, shown in Fig. S6 through to Fig. S9.† At constant light excitation for 28 min, there was no absorbance change observed (Fig. S10†). Overall, the constant results over the testing period reflects the high stability of our formulation and synthesis method.

For MSOT interrogation of the sonophores, we prepared tissue mimicking phantoms, as described in the Methods

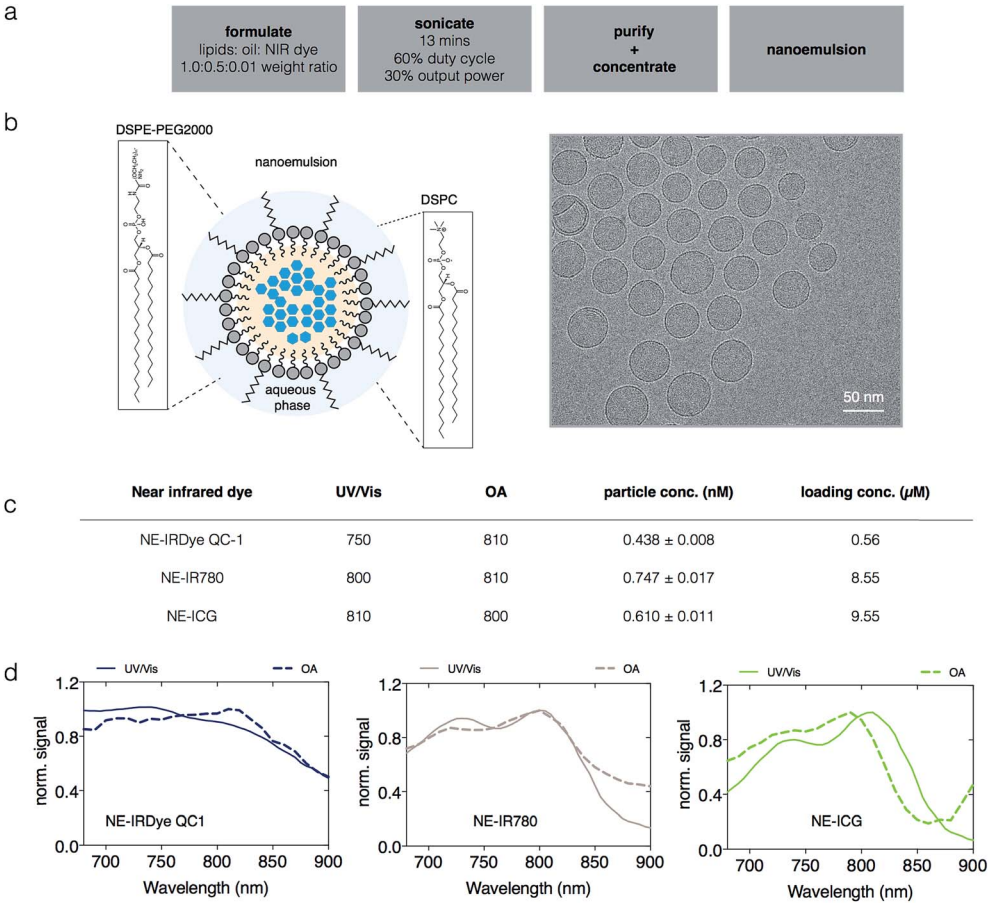

Fig. 2 Synthesis, structure, and optoacoustic spectra of selected nanoemulsions. (a) Nanoemulsions were synthesized *via* a solvent displacement method using the sonicator for 13 minutes, followed by purification and volume reduction for a more concentrated suspension. (b) Schematic diagram of nanoemulsions containing lipids, oil and sonophores (left). Morphology was determined using cryogenic electron transmission microscopy (cryo-TEM). (c) Photophysical characterization and (d) optoacoustic spectra of nanoemulsions. The nanoemulsions exhibit variability between the UV/Vis and optoacoustic spectra.

section. Subject to the Beer–Lambert's law, and similar to spectrophotometry, light is absorbed and attenuated as we probe deeper into media or tissues with optoacoustic systems.[35] To model this in our phantoms, Direct Red 81 was used to mimic optical absorption of soft tissue. To investigate any potential spectral coloring due to fluence variation for respective wavelengths of our soft tissue mimicking phantom, we examined OA and UV/Vis spectra of Direct Red 81 at varying concentrations (10 μM, 5 μM, 3 μM, 2 μM and 1 μM). The attenuation of the incident light due to the phantom was found to be negligible in the spectral region of interest compared to the high intensities of the sonophores in our phantoms, shown in Fig. S11.† The phantoms featured a series of pouches, enclosing a serial dilution of a sonophore (dye or NE concentrations were tested: high (1×), medium (1/2×) and low (1/4×) concentration), as well as a pouch filled with ICG (3 μM in DMSO) as an internal standard. Image reconstructions of the phantoms are displayed in Fig. S12 and S14.† Shown in Fig. 2, the recorded optoacoustic spectra of selected NE-IR780, NE-IRDye QC1 and NE-ICG were found to slightly deviate from their UV/Vis spectra. The same is true for all other near-infrared nanoemulsions (Fig. S13†). Additionally, we observed spectral differences for the dyes in solution *vs.* the dyes encapsulated in nanoemulsions, recorded both with UV/Vis and MSOT (Fig. S13, S15 and Table S1†). The quantitative OA signal changes when near-infrared dye is in solution (PBS) or in nanoemulsion are tabulated in Fig. S16.†

Spectral unmixing, visualization and quantification

We used several different spectral deconvolution methods to process the MSOT data from one of the tissue mimicking phantoms loaded with a nanoemulsion, NE-DYQ700. Our ultimate goal was to compare the signal specificity inferred by each method, particularly when it comes to signal quantification. Namely, the following linear regression methods were used: (1) direct classical least squares (DCLS) using (a) UV/Vis absorbance or (b) optoacoustic (OA) reference spectra; (2) non-negative least squares (NN-LS); as well as blind unmixing methods: (3) principal component analysis (PCA), and (4) independent component analysis (ICA).[36–38] The results obtained from these different techniques are shown in Fig. 3. Using the compounds' UV/Vis absorbance spectra as the

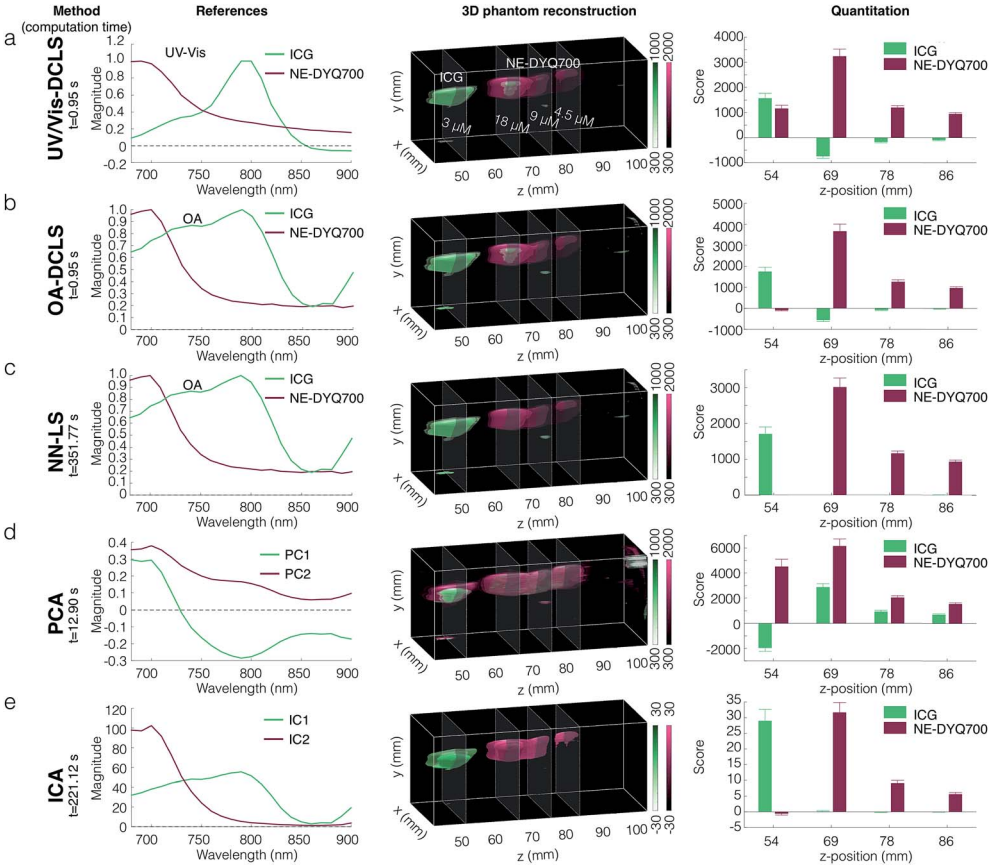

Fig. 3 Spectral unmixing, three-dimensional visualization, and quantification in tissue mimicking phantoms. Tissue mimicking phantoms with a serially diluted sample near-infrared nanoemulsion (NE-DYQ700, maroon) and ICG (3 μM, green) were analyzed, using different numerical algorithms for spectral unmixing: from top to bottom DCLS (a and b), NN-LS (c), PCA (d), and ICA (e). Reference spectra (left column) were either provided by the user (for DCLS-based methods) or derived from the dataset (for PCA and ICA, d and e respectively). The quality of the 3D visualization (middle column) depends on the methodology employed. Signal quantification produced from selected slices (right column) indicates whether the agents were identified appropriately by each method. Numerically demanding methods (NN-LS and ICA) produced fewer false positives, at the expense of computational time. For the DCLS algorithms the reference spectra acquired from the MSOT produced more specific results than the UV-Vis spectra, using the same mathematical method.

references for DCLS fitting was found to yield false positive results – *e.g.* NE-DYQ700 signal in the ICG location (Fig. 3a). The detection specificity improved when we used the OA spectra of NE-DYQ700 and ICG as references (OA-DCLS, Fig. 3b). Both methods were fast, requiring computation times of about 1 s. With the same set of OA references, NN-LS provided considerably better spectral deconvolution and signal quantification (Fig. 3c). This algorithm, however, required much higher computation time (~350 s). PCA, taking ~13 s, did not readily discriminate between NE-DYQ700 and ICG in our MSOT phantom, providing a confused signal, whereas ICA performed decidedly better, with high specificity, although at the cost of computational time (~220 s).

Nanoemulsion performance as optoacoustic agents

Through our phantom studies, we compared the performance of the different small molecules and nanoemulsion sonophores. Quantitation of the unmixed data was derived from a region of interest (ROI) at a z-slice, as indicated in the Fig. S12 and S14.† The detected OA signal intensity does not depend on NE yield nor the dye encapsulation efficiency, as shown in Fig. 4a and b and in Fig. S17.† ICG, for example, while having the highest encapsulation efficiency, only yielded moderate OA signal intensities. In order to compare the performance of the different NEs, all OA signals, after spectral deconvolution, were normalized to the intensity of the ICG standard. In Fig. 4c, the standardized intensities are seen, weighted by the concentration of encapsulated dye (left) and concentration of NE (right). Similarly, in Fig. S17† the non-encapsulated free dyes are compared against each other.

For the encapsulated dyes, it was found that per molecule weighted signal was best with the dark quencher NE-IRDye QC1 (5.66), whereas low fluorescent NE-Cy7.5 was performing the worst (0.30). When we consider per nanoparticle weighted signal, it was best with NE-DiR (15.85), whereas NE-Cy7 was performing the worst (4.26). The second highest optoacoustic signal was obtained from NE-ICG when normalizing for the nanoparticle concentration (12.51). However, this appears to be the result of the dye's high encapsulation yield. When we corrected for the concentration of encapsulated dye, or examined

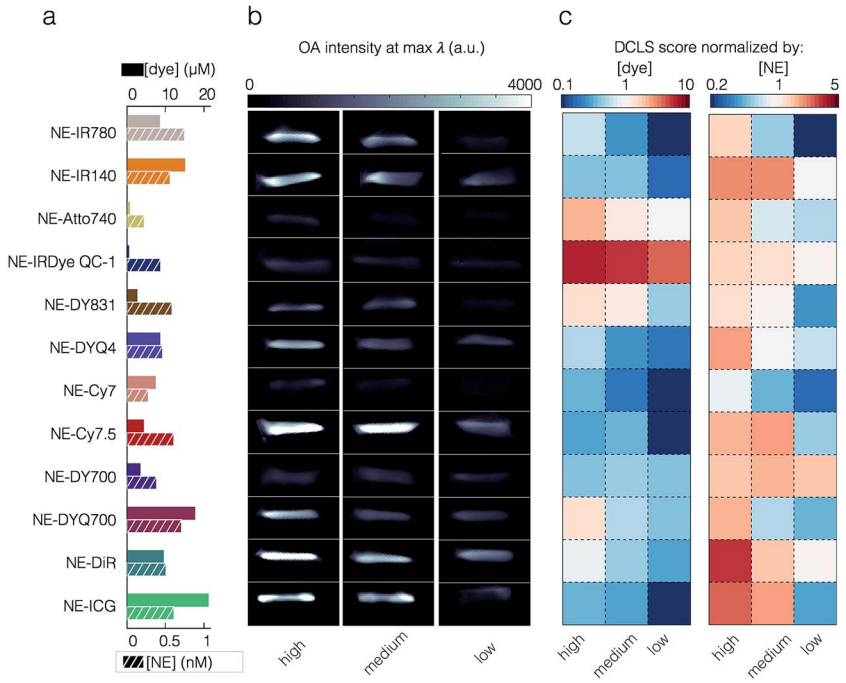

Fig. 4 Optoacoustic library and characterization of our near-infrared nanoemulsions (NEs) in tissue mimicking phantoms. (a) A library of near-infrared NEs encapsulating different sonophores was synthesized. The amount of sonophore per volume of formulation for each dye was measured post synthesis. (b) MSOT imaging of phantoms comprised of a serial dilution of the near-infrared NE was performed, with ICG (3 μM) included as a reference standard. The optoacoustic intensity is shown at the maximum peak absorbance wavelength for each NE. (c) After spectral unmixing, the nanoemulsion signal was normalized by the ICG signal and the sonophore concentration (left), to reveal the OA efficiency of each dye in the nanoemulsion or normalized by nanoemulsion concentration (right) to reveal the OA efficiency of each nanoemulsion.

the optoacoustic intensity of the free dye, the ICG performance dropped significantly (0.36 when corrected for the dye in NE and 0.87 for free dye).

Nanoemulsions as tumor-imaging agents

To assess the feasibility of NEs for cancer imaging, we tested NE-IRDye QC1 and NE-IR780 in a subcutaneous 4T1 breast

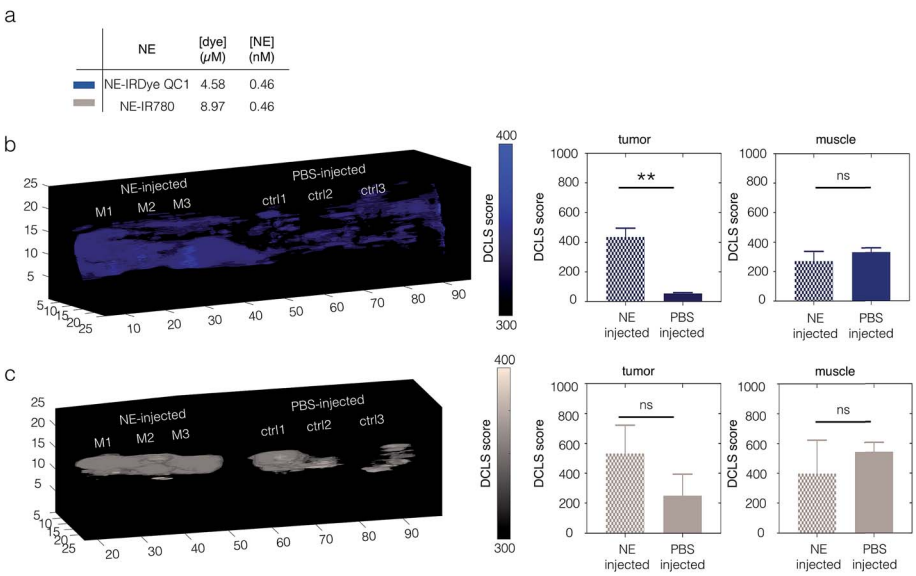

Fig. 5 *Ex vivo* MSOT imaging of tumors excised from 4T1 breast cancer mouse models. Data was acquired 24 h after intravenous injection with NE-IRDye QC1 or NE-IR780. (a) The dye and particle concentration of nanoemulsion NE-IRDye QC1 and NE-IR780 administered. (b) *Ex vivo* optoacoustic image reconstruction of excised tumors from animals injected with NE-IRDye QC1 or saline (left) and quantifications (right) of signal acquired from non-injected and injected groups. (c) *Ex vivo* optoacoustic image reconstruction of excised tumors from animals injected with NE-IR780 or saline (left) and quantifications (right) between the PBS-injected and injected groups.

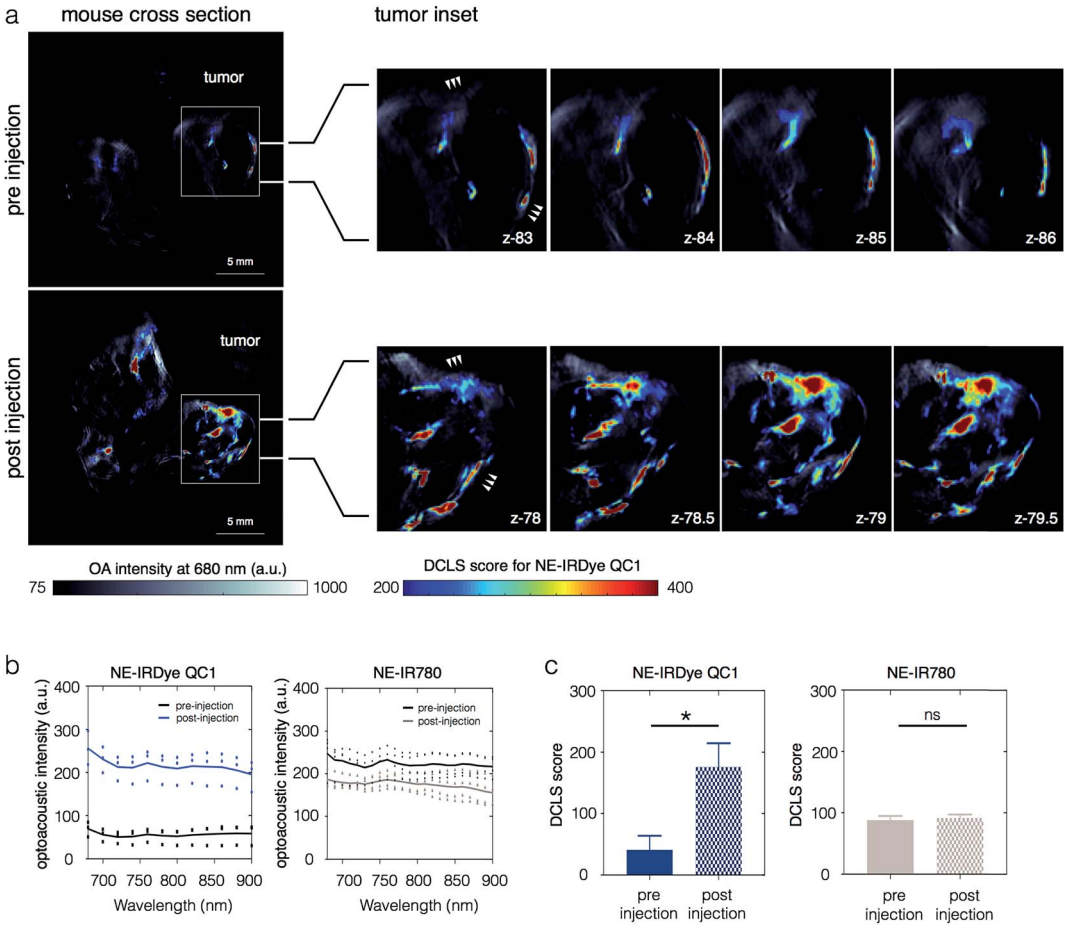

Fig. 6 *In vivo* accumulation of nanoemulsion (NE) IRDye QC1 in a 4T1 tumor model. Data was acquired 24 h after intravenous injection monitored using multi-spectral optoacoustic tomography (MSOT). (a) Transverse MSOT image of a 4T1 tumor-bearing mouse ($n = 3$) using 680 nm illumination wavelength (bone color scale) as background. MSOT images (left) are shown before (timepoint, $t = 0$ h) and after (timepoint, $t = 24$ h) injection of NE IRDye QC1 and overlaid with the NE-IRDye QC1 DCLS scores (jet color scale). Several axial positions were imaged and the tumor insets (right) are from the four different positions showing the distribution of NE-IRDye QC1 throughout the tumor. (b) The optoacoustic spectra collected at the tumor region before and after NE-IRDye QC1 injection (left) compared to NE-IR780 (right). (c) Corresponding optoacoustic signal quantification of *in vivo* MSOT images. Optoacoustic spectra of injected NE-IRDye QC1 was used as the reference, obtained from phantom experiments.

cancer allograft mouse model. These dyes were selected, as in our phantom experiments NE-IRDye QC1 was found to provide the highest OA signal (normalized by concentration of encapsulated dye), whereas NE-IR780 performed moderately.

To determine the optimal imaging timepoint, *in vivo* positron emission tomography (PET) of the radiolabelled ^{89}Zr-NE-IR780 at different timepoints (4 h, 8 h, 24 h, 48 h and 72 h) were carried out. In Fig. S18,† the results showed maximum accumulation of nanoemulsion at 24 h.

Tumor-bearing mice were intravenously injected with each NE ($n = 3$) at equal concentration (0.46 nM, 200 μL, Fig. 5a). Two control groups ($n = 3$ each) were injected with PBS. After 24 h circulation time, the mice were euthanized and selected tissues (tumor, liver, spleen and muscle) were excised and imaged with MSOT. Shown in Fig. S19,† histological analysis NE-IRDye QC1 revealed no toxicity at 24 h post injection of the nanoemulsion. Shown in Fig. S20,† the nontoxic nature of the nanoemulsions is further corroborated with *in vitro* cell viability test. For mice injected with NE-IRDye QC1, MSOT imaging of excised tumors revealed higher intensities and OA-DCLS scores compared to the control group (see Fig. 5b and S21). The mean ratio of OA-DCLS scores between injected to non-injected mice was 7.6 ± 2.2 (Fig. S21†). For NE-IR780 the average signal was higher for the injected group, however, the injected to non-injected signal ratio was not statistically significant ($p = 0.11$, Fig. 5c). When looking at the intensities and scores derived from muscle tissue, there were no statistically significant differences between the NE-injected and PBS-injected groups for either NE-IRDye QC1 ($p = 0.2$) or NE-IR780 ($p = 0.34$), and the OA-DCLS score ratios were 0.82 ± 0.12 and 1.34 ± 0.09, respectively. The corresponding ratios for liver and spleen for the nanoemulsions and blood components are shown in the Fig. S21.†

In vivo imaging with nanoemulsions

Finally, in order to evaluate the potential of NEs for eventual clinical use, we performed *in vivo* MSOT imaging, also using 4T1

allograft mouse models injected with NE-IRDye QC1 and NE-IR780. Fig. 6a shows a z-slice through a tumor, with the OA-DCLS scores overlaid on top of the optoacoustic intensities (740 nm). The OA-DCLS scores were derived in the same manner as in the phantoms. The tumor from the same animal is shown before injection (top) and 24 h after (bottom). For NE-IRDye QC1, the overall OA intensity, shown in Fig. 6b, was found to be higher in the 24 h post injection mice as compared to their pre-injected counterparts. The corresponding OA-DCLS scores, shown in Fig. 6c, were found to increase four-fold post injection ($p \leq 0.005$). Conversely, the acquired data for the NE-IR780 (Fig. S22†) show no statistically significant differences in the MSOT intensity and OA-DCLS score before and after injection ($p = 0.11$).

Discussion

In this study, we report the synthesis and validation of near-infrared optoacoustic nanoemulsions as contrast agents for tumor delineation. Our central hypothesis was that the contrast afforded by exogenous OA agents could be increased by screening and identifying better sonophore scaffolds. We therefore assembled and tested a library of dyes with NIR absorbance (680–900 nm). In addition, we wanted to provide an *in vivo* delivery system, capable of surpassing the current MSOT imaging gold standard while minimizing toxicity. Ideally, the system would be flexible and have the ability of enhancing dye solubility, bioavailability, drug loading and pharmacokinetics. In order to maximize the OA signal obtained, dyes with high extinction coefficients and low quantum yields were selected and encapsulated in oil-in-water nanoemulsions. Nanoemulsions can suspend hydrophobic dyes into physiologically acceptable formulations that are stable (Fig. S3 through to Fig. S10†), allowing for intravenous administration and *in vivo* delivery. In this experimental setting, our nanoemulsions have several attractive features: (1) they allow us to suspend high concentrations of dyes in buffer for *in vivo* delivery; (2) it is widely accepted that in the case of tumor imaging, nanoparticle agents allow passive targeting through the EPR effect,[39,40] and (3) biocompatible, cost-effective materials and easy-to-implement synthesis allow possible future clinical translation.

An important finding of our study is that the photophysical properties of sonophores undergo a change when encapsulated in nanoemulsion form. Specifically, we have observed in tissue-mimicking phantom experiments that the absorption and optoacoustic spectral maxima of most of our dyes shift, depending on whether the dye is free in solution or encapsulated in nanoemulsions (Fig. 2, S13 and S15†). Underlying reasons for this shift could be changes in the dielectric constant of the medium or the local dye concentration inside the NE. As there is a considerably higher number of dye molecules in a nanoemulsion packed into a smaller space, we expect this to lead to changes in π-stacking and cause H- and J-aggregate stacking.[41–43] This effect has also been reported in highly π-conjugated systems such as our selected cyanine dyes. In many cases, π-stacking can cause self-quenching which leads to decreased or zero fluorescence. Apart from quencher DYQ700, we observed that all quenchers increase in optoacoustic signal per molecule when they are in nanoemulsion. In all cases for fluorescent dyes, optoacoustic signal intensity per molecule decreases when they are packed in nanoemulsion. These observations are compatible with the reasoning that π-stacking is the main cause behind the spectral shift. The OA signal change due to molecular stacking in nanoemulsions is quantified and shown in Fig. S16.†

When it comes to the specific detection of sonophores, spectral analysis techniques become important.[35–38] Spectral unmixing is particularly necessary in an *in vivo* setting, with complex anatomy, biological variation, and intrinsic sonophores (*e.g.* hemoglobin) that potentially produce high background signal.[44] Using phantoms, we have performed and compared different spectral unmixing methods shown in Fig. 3. Initially, spectral unmixing was performed using DCLS. When using UV/Vis absorbance spectra as references for the DCLS fitting, we observed a high rate of false positive signals (Fig. 3a). We attribute this effect to the differences between the UV/Vis absorbance and the OA spectra, which can lead to false-positive signal reconstruction. Using the optoacoustic spectra as references for DCLS, we were able to obtain more accurate reconstructions of our phantoms (Fig. 3b), especially with regards to signal quantitation. Expanding on this, we tested a more sophisticated unmixing algorithm, namely NN-LS—a linear programming technique, where the results of the least-squares fitting are constrained only to positive numbers. While yielding more accurate image reconstruction than non-constrained DCLS, this method is much more computationally demanding, and in our particular example this analysis required more than 350 times as long to compute. We also tested methods for blind source unmixing, namely PCA and ICA. Such methods do not require the user to provide reference spectra, but instead express the data using the most important features derived from the dataset itself. Using PCA on our phantom setup (Fig. 3d), the first two principal components, capturing the bulk of our sample variance, do not clearly correspond to the individual spectra of our dyes—instead, they are a linear superposition of the two. Additionally, PCA requires the dataset to be mean-centered at zero, which makes the derived principal components hard to compare to known spectra, and also produces negative values. With ICA, which maximizes the orthogonality of the derived components, we were able to obtain a faithful reconstruction of our phantom (Fig. 3e). The quantitation of results, however, had a different scale than the other methods we employed. The reason for this is that similar to PCA, ICA requires the dataset to be pre-processed by "whitening". Whitening generates uncorrelated components with variance of unity, but at the same time, this scaling distorts the original sample units and makes quantitative comparison between different components more involved. An additional potential problem with ICA is that the algorithm depends on an initial guess, giving rise to the possibility of converging to a local optimum instead of the global solution. Ultimately, we decided on a compromising method that gives reasonable results within reasonable time, and is easy to interpret and user-friendly, namely OA-DCLS. This method does

not completely eliminate false positive regions; after spectral unmixing of animal or phantom scans, false-positive signals were identified in areas of high blood signal, or air-pockets.

To compensate for any day to day variation of the MSOT acquisition, we have used an internal standard (ICG) in all tissue mimicking phantom experiments (Fig. S12 and S14†). Having standardized our methodology for data acquisition and image analysis, we proceeded to compare our NEs, as shown in Fig. 4. As synthesized, different dyes resulted in different NE concentrations as well as different dye encapsulation yields. We have not observed a relationship between the hydrophobicity and percentage encapsulation yield of dye. Using a library screening approach, we observed that while NE-DiR offers the highest optoacoustic intensity as a function of nanoemulsion concentration, NE-IRDye QC1 outperforms the other nanoemulsions in terms of per molecule OA signal. We selected this method of quantification as we expect our ability to control and increase the encapsulation yield to improve. One method of achieving this is by changing the ratios of lipids, oil, and dye.

When we tested our NEs in *in vivo* cancer imaging settings, NE-IRDye QC1 was able to delineate tumors in a 4T1 breast cancer allograft mouse model. IRDye QC1 is non-fluorescent and features a high extinction coefficient and broad near-infrared UV/Vis and optoacoustic spectra – all favorable characteristics of an optoacoustic agent. We compared the performance of this sonophore to another NE with moderate performance, namely NE-IR780. We administered the same molar concentration of NEs to two groups of animals, all bearing subcutaneous 4T1 tumors. Although the nominal dye concentration encapsulated in the NE-IRDye QC1 formulation was approximately half of the one in NE-IR780, NE-IRDye QC1 outperformed NE-IR780 for both imaging live animals and excised tumors, corroborating the results obtained from phantom imaging.

In the case of excised tumors, imaged *ex vivo*, both NEs served to increase the OA signal *vs.* tumors from non-injected animals, as shown in Fig. 5. NE-IRDye QC1 (Fig. 5b) gave statistically significant difference ($p < 0.005$), whereas for NE-IR780 (Fig. 5c) the increase in signal was not statistically significant ($p = 0.11$).

When imaging live animals, the difference between the two agents was even more pronounced, as NE-IR780 did not provide sufficient contrast to outline the tumors before and after imaging ($p = 0.59$, Fig. S22†). NE-IRDye QC1, however, was detected within the tumors, causing a significant increase in signal between the pre- and post-injection scans in the same animal ($p = 0.015$).

Nanoemulsions provide a realistic and clinically translatable solution to the delivery of hydrophobic agents such as NIR dyes *in vivo*.[45] Derivatives of nanoemulsions, aiming to improve drug solubility in water, are already approved for clinical applications in various countries. Examples include Neoral (Novartis, Pharma, France), Propofol Lipuro (B Braun AG, Germany) and Medialipide (B Braun, France).[46]

Our approach was to maximize the impact of molecular OA imaging by delivering sonophores encapsulated within nanoemulsions. This approach indicated that ICG-based optoacoustic imaging probes may not be the most effective agents for generating strong signal. The assembly and screening of an optoacoustic library based on poorly performing fluorescent dyes allowed us to identify alternative, more promising sonophores. The development of our nanoemulsions with low fluorescent or dark sonophores for optoacoustic imaging allowed us to image tumors *in vivo*.

Conclusions

Nanoemulsions as optoacoustic sonophores have the potential to provide non-invasive imaging of tumors. Here, the development of an optoacoustic library for screening a variety of sonophores allowed us to quickly identify the best performing optoacoustic agents. Additionally, by working towards the standardization of optoacoustic image analysis, specifically for spectral unmixing, we aimed to identify optimal methods for the deconvolution of the OA data.

Specifically, we observed that there are stark variations in sonophore performance, highlighting the importance of developing new and better contrast agents for this technology. Nanoemulsions provide a stable and facile solution for the delivery of hydrophobic agents to tumors. We have demonstrated in a 4T1 mouse allograft model of breast cancer that NE-IRDye QC1 is a highly potent OA imaging agent. Not only is our nanoemulsion platform suitable for NIR optoacoustic imaging, but also could ultimately allow theranostic applications, when combined with therapeutic pharmaceuticals. Our nanoemulsions, as optoacoustic agents, have the potential to translate to other areas of optoacoustic imaging, encompassing other cancer types and allied diseases.

Materials and methods

Phospholipids were purchased from Avanti Polar Lipids (Alabama, USA). Near-infrared dyes DY831, DYQ4, DY700 and DYQ700 were purchased from Dyomics GmbH (Jena, Germany). The dye Atto740 was purchased from Atto-Tec GmbH (Siegen, Germany). IRDye QC-1 carboxylic acid was purchased from LI-COR (Cambridge, UK). Cyanine7 carboxylic acid (Cy7 COOH) and Cyanine 7.5 carboxylic acid (Cy7.5 COOH) were purchased from Lumiprobe (Florida, USA). 1,1′-Dioctadecyl-3,3,3,3′-tetramethylindotricarbocyanine iodide, DiR was purchased from Thermo Fisher Scientific (Waltham, MA, USA). Matrigel was purchased from Fisher Scientific. Cell culture media were prepared by the MSKCC Media Preparation Facility. All other reagents were purchased from Sigma-Aldrich, unless specifically stated otherwise.

Preparation of nanoemulsions

The stock solutions of low fluorescent near-infrared dyes, IR780, IR140, Atto740, DY831, Cy7 COOH, Cy7.5 COOH, DY700, DiR and ICG and dark quenchers IRDye QC1 COOH, DYQ4 and DYQ700 were dissolved in DMSO and diluted to final concentrations of 2 μM (low), 3 μM (medium) and 5 μM (high). Clear plastic straws were filled with dye solutions, sealed (KF Impulse

Hand Sealers, KF-300H, Sealer Sales, USA), and embedded in agar phantoms as described in tissue mimicking phantom section. We formulated the near-infrared dyes in nanoemulsion (NE) form adapting a previously described method.[34] First, a lipid stock solution composed of 1,2-diestearoyl-*sn*-glycero-3-phosphocholine (DSPC), pegylated DSPE (DSPE-PEG2000) and cholesterol in a 62 : 5 : 33 molar ratio was prepared in EtOH (25 mg mL^{-1}). For all phantom preparations and starting with 130 μM of dye, non-functionalized nanoemulsion composed of lipids, MCT (miglyol® 812 N, Oleochemicals, IOI group GmbH, Germany), and near-infrared dye in a 0.5 : 1 : 0.01 weight ratio were mixed together. First, the oil and the dye were mixed, followed by the addition of the lipids. Volumes were made up to a 1000 μL (EtOH) if necessary. *Via* a solvent displacement and diffusion method, the nanoemulsion was prepared by swiftly injecting 1 mL of the ethanolic mixture onto a 20 mL of PBS, immersed in an already set-up ultrasonication (Branson cup horn 150 microtip equipment, Branson Ultrasonics, USA) cold bath. Ultrasonication was carried out for 13 min for our nanoemulsion preparation using 60% DC and 30% output power, or continued until it reached the desired droplet size and/or it became constant size, typically up to 23 minutes. The nanoemulsion was purified *via* several steps. First, through centrifugation using 4000 rpm at 22 °C for 30 min to remove possible aggregates. A KrosFlo® Research Il Tangential Flow Filtration System fitted with a mPES MicroKross® modules 100 kDa MWCO (20 cm^3) was used to concentrate down to a total volume of 2000 μL. If necessary, a 100 kDa MWCO centrifugal viva spin was used for further washing steps and reducing volumes. The formulation was passed through a PES syringe filter (0.22 μm, 13 mm diameter, Celltreat Scientific Products, Pepperell, MA) before characterization or administration. Consistency within the preparation itself is required in order to compare NIR nanoemulsions to each other. For *in vivo* studies, nanoemulsion preparations were formulated with lipids, MCT (miglyol® 812 N), and near-infrared dye in a 0.5 : 1 : 0.04 weight ratio. The starting dye concentration was 520 μM.

Radiosynthesis of ^{89}Zr-NE-IR780

The synthesis of phospholipid-chelator DSPE-DFO was prepared according to our previously described procedure.[47] DFO-bearing NE-IR780 nanoemulsion was synthesized similar to the method mentioned above. 0.3% of the phospholipid-chelator DSPE-DFO was added to the formulation at the expense of DPPC. DFO-bearing NE-IR780 in PBS was reacted with ^{89}Zr-oxalate, incubated at 37 °C and shaken for 60 min. Free ^{89}Zr was separated by spin filtration using 100 kDa molecular weight cutoff filter (Millipore, Billerica, MA). The retentate was washed with sterile PBS (3 × 1 mL) and concentrated to the desired volume. The radiochemical yield was 72% and radiochemical purity >99% (Fig. S20†).

HPLC and Radio-HPLC

High-performance liquid chromatography (HPLC) was performed on a Shimadzu HPLC system equipped with two LC-10AT pumps and an SPD-M10AVP photodiode array detector. Radio-HPLC was performed using a Lablogic Scan-RAM Radio-TLC/HPLC detector. Size exclusion chromatography (SEC) was performed on a Superdex 10/300 column (GE Healthcare Life Sciences, Pittsburg, PA) using PBS as eluent at a flow rate of 1 mL min^{-1}.

Characterization of nanoemulsions

Absorption and fluorescence spectra were measured in a 96-well plate (Corning™ Costar™ black clear bottom, Thermo Fisher Scientific) with path lengths of 0.231 cm and 0.300 cm for volume 75 μL and 100 μL, respectively. UV/Vis absorbance and fluorescence spectra were measured on SpectraMax® M5 Multi-Mode Microplate Reader. Samples were measured together with a corresponding reference solvent contained in a matched well and volume. Measurements were recorded in triplicates at 25 °C. The absorbance scan was performed with an integration time of 0.5 seconds and range from 350 nm to 1000 nm in 5 nm steps.

Spectra and linear calibrations were plotted using Prism 7 (GraphPad Software, La Jolla, CA, USA). Encapsulation efficiency was determine by preparing a 300 μL of nanoemulsion aliquot in an amber vial, lyophilized (FreeZone 2.5 Plus, Labconco, Kansa City, MO, USA) and re-suspended in 300 μL DMSO. Defaced sample was passed through a PES syringe filter (0.22 μm, 13 mm diameter, Celltreat Scientific Products, Pepperell, MA) before measuring its UV/Vis absorption. Using our equation from the plotted standard curve and based on the absorbance maxima measured (Fig. S2†), the unknown concentration of dye was calculated. The size distribution and zeta potential of the nanoemulsions were determined by DLS (Malvern Instrument Ltd., UK). The nanoparticle concentration was determined using the nanoparticle tracking analysis, NTA (NanoSight Ltd, UK).

The morphology of the nanoemulsion NE-IRDye QC1 was determined using cryogenic transmission electron microscopy (cryo-TEM) adapted from previously described method.[48,49] Briefly, 3 μL of the prepared NE-IRDye QC1 were pipetted onto the grid, blotted for 1.5 s on grade 595 filter paper and immediately plunge-frozen using FEI Vitrobot Mark V (FEI, Hillsboro, OR) with 4 °C chamber and 70% humidity settings. NE-IRDye QC1 were screened and imaged in a FEI Titan Krios G2 microscope (FEI, Hillsboro, OR), equipped with an XFEG operating at 300 kV. Data collection was automated using SerialEM,[48] with images taken at nominal magnification of 18 000×, electron dose rate of 10 electrons per px per s and defocus of −2 μm. 8 s exposures were collected at super-resolution movies using a Gatan K2 summit direct electron detector, at super-resolution of 0.571 Å px^{-1}. Movies were drift-corrected using MotionCor2 (ref. 49) and downsampled *via* binning by 2 to pixel size 1.14 Å px^{-1}.

Tissue mimicking phantom preparation

To assess optoacoustic detection of the nanoemulsion spectra under controlled conditions, we imaged nanoemulsion samples embedded in a cylindrical, light-scattering phantom. For simulating the tissue background in biological systems, we created soft tissue mimicking phantoms by combining two

methods to produce an acoustic attenuation of 0.495 dB cm^{-1} MHz^{-1}, all according the generic tissue definition given by Cook *et. al.*[20,50] Specifically, soft tissue mimicking phantoms were freshly prepared by adding 15% v/v intralipid® 20%, I.V. fat emulsion to provide the scattering and 0.01 mM Direct Red 81 for absorption to a pre-warmed solution of 1.5% v/v agarose Type 1 (solid in <37 °C) in Milli Q water (18.2 MΩ cm at 25 °C). The solution was poured into a 20 mL syringe (2 cm diameter) serving as a plastic mold to create a cylindrical shape of the phantom, into which a sealed thin walled optically clear plastic straw containing the nanoemulsion or dye of interest was inserted. To compare their relative optoacoustic imaging potential, we have prepared three serial dilutions of the nanoemulsions: high (1×), medium (1/2×) and low (1/4×). The phantoms were allowed to cool at room temperature until the agarose solidified. Clinically relevant and commercially available small molecule near-infrared dyes (IR780, IR140, Atto740, IRDye QC1, DY831, DYQ4, Cy7, Cy7.5, DY700, DYQ700, and DiR) were prepared and measured in DMSO and their corresponding nanoemulsions were measured in phosphate buffered saline for the MSOT phantom studies.

Cytotoxicity assessment of nanoemulsions

Murine breast cancer 4T1 cells were grown and maintained in Dulbecco Modified Eagle Medium (DMEM) containing 10% fetal bovine serum (FBS) under standard cell culture conditions of 5% CO_2 in air at 37 °C. *In vitro* toxicity testing of 4T1 cells (100 000, 300 000 and 500 000) were loaded with 1 μM of NE-IR780 or NE-IRDye QC1. Cell viability tests using trypan blue were performed at 30, 60 and 120 min timepoints and using automated cell counter (Vi-Cell Cell Viability Analyzer, Beckman Coulter, IN, USA).

For *in vitro* survival test, 200 cells per well were seeded and maintained in clear bottom 96-well black plate (Greiner Bio-One GmbH, Germany) for 2 days. The media was replaced with 200 μL of varying concentrations of nanoemulsions (1 μM, 2 μM and 3 μM), prepared in DMEM and allowed to incubate for 24 h. The solution mixtures were replaced with DMEM and waited 48 h. The media was replaced with 20% v/v of alamar blue in DMEM which lacks phenol red and serum and incubated for 4 h, followed by UV/Vis and fluorescence measurements. Positive controls are cells with alamar blue without prior nanoemulsion treatment and the negative controls were alamar blue added to medium without cells.

After imaging, livers and tumors were harvested and fixed in 4% paraformaldehyde (PFA, MP Chemicals, Solon, OH) in PBS overnight at 4 °C, thoroughly rinsed with PBS, then kept in 70% ethanol. Tissues were embedded in paraffin and 5 μm thick sections were sliced from the paraffin block. The sections were stained with hematoxylin and eosin (H&E) and scanned with Mirax digital slide scanner (Zeiss, Jena, Germany) for histological analysis.

Optoacoustic imaging

A pre-clinical multi-spectral optoacoustic tomography (MSOT) device (MSOT inVision 256, iThera Medical, Munich, Germany) equipped with an array of 256 detector elements which are cylindrically focused, having a central ultrasound frequency of 5 MHz and up to 270° coverage, was used for imaging. The phantoms were aligned so that the illumination ring coincides with the detection plane, *i.e.* the curved transducer array being centered around the phantom. Data acquisition was performed in the wavelength range 680–900 nm in 10 or 20 nm steps, using 10 averages per wavelength, which equates to 1 s acquisition time per wavelength per section. The optical excitation originates from a Q-switched Nd:YAG laser with a pulse duration of 10 ns and a repetition of 10 Hz. Light is homogenously delivered to the phantom using a fiber split into 10 output arms. The fiber bundle and the transducer array are stationary and the sample holder moves along the *z*-direction allowing longitudinal acquisition of different imaging planes using a moving stage. MSOT measurements were performed in a temperature controlled water bath at 34 °C. During the measurements all of the variable parameters were kept constant, *i.e.* optoacoustic gain, laser power, focus depth, frame averaging, and frame rate. We waited at least 5 min before initiating the scan, so that the phantom equilibrates to the temperature of the water bath before measurement, for optimal acoustic coupling.

Optoacoustic image data processing

Spatial reconstruction of the data was performed using the ViewMSOT software suite (V3.6; iThera Medical) and a back-projection algorithm. The data were then transferred to MATLAB (R2017b) and subsequent analysis was performed using a GUI developed in house. The normalized optoacoustic reference spectra (such as the ones shown in Fig. 3, S3 and S6 were obtained from optoacoustic phantom scans). Scans were performed from 680 to 900 nm with 10 nm steps and the spectra were normalized to their respective optoacoustic signal maxima (see Table S1†). To generate the DCLS models for *in vivo*, *ex vivo*, and *in vitro* studies, the reference optoacoustic spectra of the NE phantom were used. For the investigation of spectral unmixing the analysis was performed as follows: DCLS by using a Moore–Penrose pseudo-inverse matrix of the reference spectra; NN-LS with the PLS Toolbox v.8.0 (Eigenvector Research, Inc., Wenatchee, WA, USA); PCA using the PCA function in MATLAB; and ICA using the fastica package in Matlab.[51] To compare computational times, all methods of spectral unmixing were performed under identical conditions (Macbook, 2.4 GHz Intel Core i5, 16 Gb 1600 MHz DDR3, macOS Sierra and Matlab 2014b). The three-dimentional (3D) image reconstructions of the phantoms were shown were produced with 50 isosurfaces. Quantitative image processing of the data was performed by defining the region of interest within a 2D slice ($n = 3$) MSOT image.

Data analysis

DCLS scores were extracted from z-slices ($n = 3$), as indicated by frames. For *ex vivo* imaging experiments, unpaired *t*-tests were carried out between injected and non-injected mice. For *in vivo* imaging experiments, paired *t*-tests between the pre-injection and post-injection were carried out. In the case of *ex vivo* experiments, signal ratios were calculated by dividing the average

signal of the non-injected control group with the average signal of the injected group. In the case of *in vivo* experiments, signal ratios were calculated by dividing the pre/post signals in the region of interest (ROI) selected prior to injection.

Animal studies

All animal experiments were done in accordance with protocols approved by the Institutional Animal Care and Use Committee (IACUC) of Memorial Sloan Kettering Cancer Center (MSKCC) and followed the National Institutes of Health guidelines for animal welfare. Healthy Hsd:athymic female mice Nude-Foxn1^{nu} (6–8 weeks old) were used in the study. All animal procedures, other than tail vein injections, were performed with the animals under general 2% isoflurane inhalation anesthesia. In order to test the ability of nanoemulsions to target tumor tissue, subcutaneous allografts were created using mouse breast cancer cell line 4T1. The 4T1 cells were injected (1×10^6 cells in 150 μL 1 : 1 RPMI medium and Matrigel) into the lower right flank. The tumors were allowed to grow for 6–7 days (typically reaching a volume estimated from caliper measurements of 3–5 mm^3) before the nanoemulsion formulation were injected. 200 μL of 155–229 mg kg^{-1} (dye basis) nanoemulsion formulation/phosphate buffered saline solution were injected into mice *via* tail vein. The nanoemulsions were injected and allowed to circulate for 24 h to study and assess the distribution and accumulation of the contrast agent.

Ex vivo optoacoustic experiments

In *ex vivo* MSOT experiments, a total of seven female homozygous Hsd:athymic mice Nude-Foxn1^{nu} (6–8 weeks old) were used for each cohort of experiment. The cohort were split into two groups, namely injected ($n = 4$) and non-injected (control, $n = 3$) groups. The injected group was intravenously injected with nanoemulsions (200 μL of 155–229 mg kg^{-1}) 24 h before the animals were sacrificed by CO_2 asphyxiation, followed by cervical dislocation. At 24 h post injection, major organs of the injected and non-injected cohort (tumor, liver, spleen and muscle) were harvested and imaged with MSOT for *ex vivo* biodistribution assessment. Organs were imaged in groups (injected and non-injected together) and in one measurement. Ultrasound colorless gel (approximately 0.5–1 mm thick layer) was applied onto the clear plastic membrane for improved acoustic coupling. The organs were aligned horizontally onto the clear plastic membrane, injected (left) and non-injected (right) group were aligned side by side, having sufficient spacing in between the organs, and immersed in a 34 °C water bath. OA intensities were obtained from 680–900 nm, in 10 nm wavelength step and 1 mm step size using 25 mm field of view (FOV) taking 10 averages per frame.

In vivo optoacoustic experiments

For *in vivo* MSOT experiments, a total of four female homozygous Hsd:athymic mice Nude-Foxn1^{nu} (6–8 weeks old) were used. The mice were placed into the animal holder in supine position, gently fixed into position using clear straps and fitted with a breathing mask delivering a constant flow of 1.5–2% isoflurane anesthesia (as described above). Ultrasound colorless gel (approximately 1–2 mm thick layer) was applied onto the mouse around the region of interest in order to improve acoustic coupling. The animal holder was closed, wrapping the clear plastic membrane around the mouse and air gaps and bubbles in between the membrane and mouse's skin were removed. The animal holder with the mouse positioned inside it was then placed into the imaging chamber, with the animal being aligned with regards to the detection plane (centered within the curved transducer array). To acquire baseline data, mice were initially scanned prior to injection of contrast agents. Animals were then administered 155–229 mg kg^{-1} of nanoemulsion formulation (concentration 0.47 nM) and scanned again 24 h post injection. The scan parameters used for imaging animals were the same as described above for imaging of phantoms. To minimize the scan duration for the animals, the spectral resolution was limited to 20 nm, and the longitudinal spatial resolution to 1 mm. The abdomen and hind limbs of the animals were scanned, with typical scan durations of approximately 13 minutes.

Author contributions

S. R., C. A. and T. R. designed the experiments and analyzed the data. S. R., C. A., C. C., P. D. and M. J carried out the experiments. M. J. C. carried out the cryo-TEM experiment. S. R., C. A., M. F. K., and T. R. interpreted data. S. R., C. A. and T. R. primarily wrote the manuscript. All authors read, provided feedback on, and approved the manuscript.

Conflicts of interests

The authors declare no competing financial interests.

Acknowledgements

The authors thank the support of Memorial Sloan Kettering Cancer Center's Animal Imaging Core Facility and Radiochemistry & Molecular Imaging Probes Core Facility. This work was supported by National Institutes of Health grants NIH 1 R01 HL125703 (W. J. M. M.), R01 CA212379 (J. G.), R01 EB017748 (M. F. K.) and K08 CA16396 (M. F. K.), R01CA204441 (T. R.), R21CA191679 (T. R. and W. W.) and P30 CA008748. M. F. K. is a Damon Runyon-Rachleff Innovator supported (in part) by the Damon Runyon Cancer Research Foundation (DRR-29-14).

References

1 A. G. Bell, *Science*, 1881, **2**, 242–253.
2 V. Ntziachristos, *Nat. Methods*, 2010, **7**, 603–614.
3 V. Ntziachristos and D. Razansky, *Chem. Rev.*, 2010, **110**, 2783–2794.
4 M. Omar, M. Schwarz, D. Soliman, P. Symvoulidis and V. Ntziachristos, *Neoplasia*, 2015, **17**, 208–214.
5 M. A. Juratli, Y. A. Menyaev, M. Sarimollaoglu, E. R. Siegel, D. A. Nedosekin, J. Y. Suen, A. V. Melerzanov, T. A. Juratli, E. I. Galanzha and V. P. Zharov, *PLoS One*, 2016, **11**, e0156269.

6 E. I. Galanzha, M. G. Viegas, T. I. Malinsky, A. V. Melerzanov, M. A. Juratli, M. Sarimollaoglu, D. A. Nedosekin and V. P. Zharov, *Sci. Rep.*, 2016, **6**, 21531.
7 J. Yao, L. Wang, J.-M. Yang, K. I. Maslov, T. T. W. Wong, L. Li, C.-H. Huang, J. Zou and L. V. Wang, *Nat. Methods*, 2015, **12**, 407–410.
8 J. Tang, L. Xi, J. Zhou, H. Huang, T. Zhang, P. R. Carney and H. Jiang, *J. Cereb. Blood Flow Metab.*, 2015, **35**, 1224–1232.
9 I. Stoffels, S. Morscher, I. Helfrich, U. Hillen, J. Leyh, N. C. Burton, T. C. P. Sardella, J. Claussen, T. D. Poeppel, H. S. Bachmann, A. Roesch, K. Griewank, D. Schadendorf, M. Gunzer and J. Klode, *Sci. Transl. Med.*, 2015, **7**, 317ra199.
10 G. P. Luke and S. Y. Emelianov, *Radiology*, 2015, **277**, 435–442.
11 V. Neuschmelting, H. Lockau, V. Ntziachristos, J. Grimm and M. F. Kircher, *Radiology*, 2016, **280**, 137–150.
12 J. Weber, P. C. Beard and S. E. Bohndiek, *Nat. Methods*, 2016, **13**, 639–650.
13 S. Roberts, M. Seeger, Y. Jiang, A. Mishra, F. Sigmund, A. Stelzl, A. Lauri, P. Symvoulidis, H. Rolbieski, M. Preller, X. L. Deán-Ben, D. Razansky, T. Orschmann, S. C. Desbordes, P. Vetschera, T. Bach, V. Ntziachristos and G. G. Westmeyer, *J. Am. Chem. Soc.*, 2018, **140**(8), 2718–2721.
14 T. Zhang, H. Cui, C.-Y. Fang, J. Jo, X. Yang, H.-C. Chang and M. L. Forrest, *Proc. SPIE*, 2013, **8815**, 881504.
15 G. P. Luke, J. N. Myers, S. Y. Emelianov and K. V. Sokolov, *Cancer Res.*, 2014, **74**, 5397–5408.
16 M. Shakiba, K. K. Ng, E. Huynh, H. Chan, D. M. Charron, J. Chen, N. Muhanna, F. S. Foster, B. C. Wilson and G. Zheng, *Nanoscale*, 2016, **8**, 12618–12625.
17 J. Laufer, P. Johnson, E. Zhang, B. Treeby, B. Cox, B. Pedley and P. Beard, *J. Biomed. Opt.*, 2012, **17**, 056016.
18 P. Beard, *Interface Focus*, 2011, **1**, 602–631.
19 K. V. Kong, L.-D. Liao, Z. Lam, N. V. Thakor, W. K. Leong and M. Olivo, *Chem. Commun.*, 2014, **50**, 2601–2603.
20 K. Haedicke, C. Brand, M. Omar, V. Ntziachristos, T. Reiner and J. Grimm, *J. Photoacoust.*, 2017, **6**, 1–8.
21 J. Levi, A. Sathirachinda and S. S. Gambhir, *Clin. Cancer Res.*, 2014, **20**, 3721–3729.
22 Y. Li, A. Forbrich, J. Wu, P. Shao, R. E. Campbell and R. Zemp, *Sci. Rep.*, 2016, **6**, 22129.
23 M. Frenette, M. Hatamimoslehabadi, S. Bellinger-Buckley, S. Laoui, J. La, S. Bag, S. Mallidi, T. Hasan, B. Bouma, C. Yelleswarapu and J. Rochford, *J. Am. Chem. Soc.*, 2014, **136**, 15853–15856.
24 S. Banala, S. Fokong, C. Brand, C. Andreou, B. Krautler, M. Rueping and F. Kiessling, *Chem. Sci.*, 2017, **8**, 6176–6181.
25 C. Yin, X. Zhen, Q. Fan, W. Huang and K. Pu, *ACS Nano*, 2017, **11**, 4174–4182.
26 C. Andreou, S. Pal, L. Rotter, J. Yang and M. F. Kircher, *Mol. Imaging Biol.*, 2017, **19**, 363–372.
27 S. Mallidi, G. P. Luke and S. Emelianov, *Trends Biotechnol.*, 2011, **29**, 213–221.
28 M. Mehrmohammadi, S. J. Yoon, D. Yeager and S. Y. Emelianov, *Curr. Mol. Imaging*, 2013, **2**, 89–105.
29 N. Beziere, N. Lozano, A. Nunes, J. Salichs, D. Queiros, K. Kostarelos and V. Ntziachristos, *Biomaterials*, 2015, **37**, 415–424.
30 R. Williams, C. Wright, E. Cherin, N. Reznik, M. Lee, I. Gorelikov, F. S. Foster, N. Matsuura and P. N. Burns, *Ultrasound Med. Biol.*, **39**, 475–489.
31 M. A. Miller, S. Arlauckas and R. Weissleder, *Nanotheranostics*, 2017, **1**, 296–312.
32 C. A. Aaron, P. Balabhaskar, P. Kapil and M. Samir, *Transl. Mater. Res.*, 2017, **4**, 014001.
33 D. Bobo, K. J. Robinson, J. Islam, K. J. Thurecht and S. R. Corrie, *Pharm. Res.*, 2016, **33**, 2373–2387.
34 C. Pérez-Medina, D. Abdel-Atti, J. Tang, Y. Zhao, Z. A. Fayad, J. S. Lewis, W. J. M. Mulder and T. Reiner, *Nat. Commun.*, 2016, **7**, 11838.
35 S. Tzoumas, A. Nunes, I. Olefir, S. Stangl, P. Symvoulidis, S. Glasl, C. Bayer, G. Multhoff and V. Ntziachristos, *Nat. Commun.*, 2016, **7**, 12121.
36 S. Morscher, J. Glatz, N. C. Deliolanis, A. Buehler, A. Sarantopoulos, D. Razansky, V. E. D. L. C. Ntziachristos and V. Ntziachristos, Spectral unmixing using component analysis in multispectral optoacoustic tomography, *Conference paper, ECBO*, OSA publishing, Munich, 2011.
37 J. Glatz, N. C. Deliolanis, A. Buehler, D. Razansky and V. Ntziachristos, *Opt. Express*, 2011, **19**, 3175–3184.
38 L. Ding, X. L. Deán-Ben, N. C. Burton, R. W. Sobol, V. Ntziachristos and D. Razansky, *IEEE Trans. Med. Imaging.*, 2017, **36**, 1676–1685.
39 T. Lammers, L. Y. Rizzo, G. Storm and F. Kiessling, *Clin. Cancer Res.*, 2012, **18**, 4889.
40 W. R. Sanhai, J. H. Sakamoto, R. Canady and M. Ferrari, *Nat. Nanotechnol.*, 2008, **3**, 242–244.
41 G. P. Bartholomew and G. C. Bazan, *J. Am. Chem. Soc.*, 2002, **124**, 5183–5196.
42 Y. Ikabata, Q. Wang, T. Yoshikawa, A. Ueda, T. Murata, K. Kariyazono, M. Moriguchi, H. Okamoto, Y. Morita and H. Nakai, *npj Quantum Materials*, 2017, **2**, 27.
43 G. P. Bartholomew and G. C. Bazan, *Acc. Chem. Res.*, 2001, **34**, 30–39.
44 S. Tzoumas, A. Nunes, N. C. Deliolanis and V. Ntziachristos, *J. Biophotonics*, 2015, **8**, 629–637.
45 A. S. Klymchenko, E. Roger, N. Anton, H. Anton, I. Shulov, J. Vermot, Y. Mely and T. F. Vandamme, *RSC Adv.*, 2012, **2**, 11876–11886.
46 N. Anton, F. Hallouard, M. F. Attia and T. F. Vandamme, Nano-emulsions for Drug Delivery and Biomedical Imaging, in *Intracellular Delivery III. Fundamental Biomedical Technologies*, ed. A. Prokop and V. Weissig, Springer, Cham, 2016, pp. 273–300.
47 C. Pérez-Medina, D. Abdel-Atti, Y. Zhang, V. A. Longo, C. P. Irwin, T. Binderup, J. Ruiz-Cabello, Z. A. Fayad, J. S. Lewis, W. J. M. Mulder and T. Reiner, *J. Nucl. Med.*, 2014, **55**, 1706–1711.
48 D. N. Mastronarde, *J. Struct. Biol.*, 2005, **152**, 36–51.
49 S. Q. Zheng, E. Palovcak, J.-P. Armache, K. A. Verba, Y. Cheng and D. A. Agard, *Nat. Methods*, 2017, **14**, 331.
50 J. R. Cook, R. R. Bouchard and S. Y. Emelianov, *Biomed. Opt. Express*, 2011, **2**, 3193–3206.
51 A. Hyvärinen and E. Oja, *Neural Netw.*, 2000, **13**, 411–430.